Modeling the dynamic behavior of a droplet evaporation device for the delivery of isotopically calibrated low-humidity water vapor

Erik Kerstel[1]

[1]Univ. Grenoble Alpes, CNRS, LIPhy, 38000 Grenoble, France

Correspondence: Erik Kerstel (erik.kerstel@univ-grenoble-alpes.fr)

Abstract. A simple model is presented that gives a quantitative description of the dynamic behavior in terms of water concentration (humidity) and isotope ratios of a low-humidity water vapor generator. The generator is based on the evaporation of a nL-droplet produced at the end of syringe needle by balancing the inlet water flow and the evaporation of water from the droplet surface into a dry air stream. The humidity level is adjusted by changing the speed of the high-precision syringe pump and, if needed, the dry air flow. The generator was developed specifically for use with laser-based water isotope analyzers in Antarctica, and recently described in Leroy-Dos Santos et al. (2020). Apart from operating parameters such as temperature, pressure, water and dry air flows, the model has as "free" input parameters the water isotope fractionation factors and the evaporation rate. We show that the experimental data constrain these parameters to physically realistic values that are in reasonable to good agreement with literature values where available.

1 Introduction

It is no overstatement to say that laser-based isotope analyzers have revolutionized the field of water isotope ratio instrumentation, until not so long ago dominated by Isotope Ratio Mass Spectrometers (e.g., Kerstel, 2004; Kerstel and Gianfrani, 2008). In particular, laser instruments have enabled continuous measurements of low-humidity atmospheric air in airborne and Antarctic field settings (see, among others, Iannone et al., 2009b, 2010; Moyer et al., 2013; Steen-Larsen et al., 2013; Casado et al., 2016; Ritter et al., 2016; Bréant et al., 2019). In order to calibrate such instruments against international standard and reference materials that are all in liquid form, it is necessary to bring these into the vapor phase without causing fractionation, or alternatively with well-controlled, quantitative fractionation, while also controlling the level of humidity (the volume mixing ratio). Several solutions have been proposed and developed into prototypes and commercial instruments, but few are capable of delivering a stable supply at low humidity levels (Iannone et al., 2009a; Sturm and Knohl, 2010; Gkinis et al., 2010; Tremoy et al., 2011). One approach is that of the instrument developed in our laboratory with the specific aim of calibrating laser-based analyzers deployed in Antarctica and first reported in Landsberg et al. (2014). This prototype instrument has undergone significant engineering developments in order to improve its performance and robustness (Leroy-Dos Santos et al., 2020). In this companion paper we provide a theoretical model that is capable of a quantitative description of its operation.

2 Modeling the syringe water isotope delivery module

25 Here we model the dynamic behavior of the water concentration (humidity) and isotope ratios of a low humidity-level generator (LHLG), such as described in the companion paper by Leroy-Dos Santos et al. (2020). The LHLG instrument uses a commercial high-precision syringe pump system (Harvard 11 Pico Plus Elite) to push in the plunger of a small-volume syringe. The needle of the syringe punctures a septum of a small evaporation chamber in which a steady air flow at a controlled pressure of 1 bar is maintained around the needle tip. Water being pushed through the syringe needle will start to form a droplet at the tip of

30 the needle, provided the water flow is sufficiently high to overcome the evaporation from the exposed water surface inside the needle. Initially, as the water cap or droplet is still small, the evaporation rate from its surface into the surrounding dry air flow is smaller than the rate of water supply and the droplet continues to grow. As the droplet grows in size, its surface area increases and so will the rate of evaporation. Once steady state is reached, the evaporation of water from the surface of the droplet at the end of the syringe is exactly matched in quantity and isotopic composition by the supply of the standard water through the

35 syringe needle.

Considering the isotopic composition of the evaporated water, it is clear that at the very beginning the isotopic composition of the meniscus (the droplet cap) equals that of the bulk water in the syringe. Also, in steady-state the isotopic composition of the vapor is identical to that in the syringe reservoir. In the transient regime, however, the isotopic fractionation occurring at the surface liquid-to-gas phase boundary implies an enrichment of the surface layer that first needs to diffuse inwards. We thus

40 expect to see a depleted vapor phase (relative to the reservoir liquid) as long as the droplet is growing. Inversely, if the water flow is reduced and the droplet shrinks, we expect to see a temporary enrichment of the vapor.

In order to model these dynamics quantitatively, and thus understand which factors control the magnitude of the transient signals, we assume a pinned, sessile droplet with the shape of a partial sphere, as shown in Figure 1.
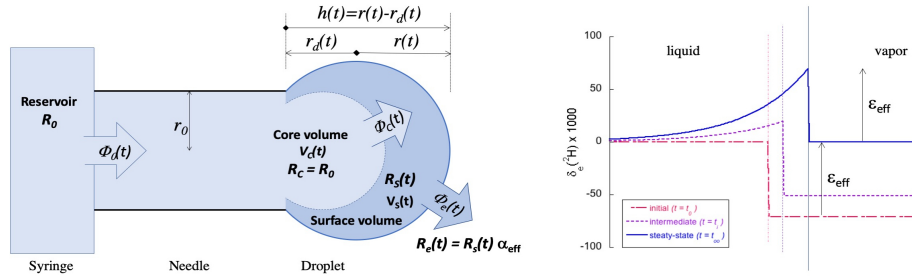
Figure 1. (a) Schematic representation of the ideal spherical droplet formed at the end of the syringe needle tip, illustrating the different reservoirs with volume V, water fluxes Φ, and isotope ratios R involved in the model. Since $r^2 = r_0^2 + r_d^2$ and $r_d = r - h$, it follows that $r = \left(r_0^2 + h^2\right) / \left(2h\right)$. (b) The isotope ratio profile over the liquid to vapor boundary (left to right, with the thin vertical lines representing the growing water surface) at three instants in time if the water flux Φ_0 from the syringe (with $\delta_0 = 0$) follows a step function with $\Phi_0(t) = 0$ for $t < t_0$, and $\Phi_0(t) = F > 0$ for $t > t_0$. The isotope fractionation is taken to be $\epsilon_{eff} \approx -71‰$ for $\delta^2\mathrm{H}$. While the droplet is growing $\delta_e < \delta_0$. At $t = t_\infty$ the incoming water flux Φ_0 equals the evaporated water flux Φ_e and $\delta_e = \delta_0$.

For completeness, we assume that only a fraction f of the droplet volume (a boundary layer) becomes enriched. This is later
45 used to demonstrate that the best model results are obtained by assuming that the entire droplet becomes enriched ($f = 1$, see section 3.1), an observation that is further supported by considerations involving the relative speeds of isotopic diffusion and the water flow (section 4.1). Figure 1(b) shows the radial isotope concentration profile inside the droplet and the neighboring vapor following a step function in the flow rate from zero to some fixed value at $t = t_0$. The actual form of the profile is not important for our model and could just as well be approximated by a square profile. We can thus distinguish four different
50 bodies of water:

1. The syringe reservoir with a constant isotope ratio R_0 and an outgoing water flux equal to $\Phi_0(t)$ determined by the syringe pump speed,

2. The core volume of the droplet with an isotope ratio $R_c = R_0$ and a time-dependent volume $V_c(t)$. The water flux from the core to the surface layer of the droplet is given by $\Phi_c(t)$. Only in steady state $\Phi_c = \Phi_0$.

55 3. A fraction f $(0 < f \leq 1)$ of the total droplet volume $V_d(t)$ that will become enriched in the heavy isotope, $V_s(t)$, with isotope ratio $R_s(t)$:

$$V_s(t) = f \cdot V_d(t) \tag{1}$$

4. The evaporated water flux $\Phi_e(t)$ leaving the droplet with isotope ratio $R_e(t) = R_s(t) \cdot \alpha_{eff}$. Here the relevant isotope fractionation factor is that between the vapor and liquid phase water: $\alpha_{eff} = (1 + \epsilon_{eff}) < 1$.

60   A last essential part of the model is the assumption that the evaporation rate is proportional to the exposed surface area of the droplet:

$$\Phi_e(t) = k_e \cdot A_s(t) \tag{2}$$

Figure 1 gives a schematic representation of our model, indicating the relevant water volumes and inter-volume fluxes, as well as the isotope ratios R of each volume. Solving the model *ab initio* is not difficult and will be shown to give a qualitatively

65   and quantitatively satisfactory description of the dynamics under realistic conditions.

The free input parameters to the model are (1) the effective liquid-to-vapor fractionation factor α_{eff}, the estimate for which we base on studies by Cappa et al. (2003) and Luz et al. (2009), (2) the fraction f of the droplet that becomes enriched, which we will show in section 3 to be equal to unity, and (3) the evaporation coefficient k_e, which in turn we base on previous work by Walton (2004) and Sefiane et al. (2009), and justify in the discussion of section 4.4.

70   The first task is to model the evaporated total water flux $\Phi_e(t)$ as a function of a variable input water flux $\Phi_0(t)$, driven by variations in the syringe pump speed. For this we write the mass balance equation for the non-compressible fluid in discrete time with time step dt:

$$V_d(t + dt) = V_d(t) + (\Phi_0(t) - \Phi_e(t)) \cdot dt \tag{3}$$

The evaporation flux $\Phi_e(t)$ is a function of the droplet size through (2). For simplicity, we model the droplet at the tip of the

75   needle as a partial sphere, a spherical cap. The surface area of the spherical-cap-shaped droplet is given by (see Figure 1):

$$A_s \equiv A_{cap} = 2\pi r h = \pi \left(r_0^2 + h^2 \right) \tag{4}$$

with the radius of curvature of the cap r, the cap height h ($0 \le h \le 2r$), and the inner diameter $2r_0$ of the needle, all as defined in Figure 1. The volume of the droplet is equally a function of h:

$$V_d \equiv V_{cap} = \frac{\pi}{6} h \left(3r_0^2 + h^2 \right) \tag{5}$$

80    $A_s(t)$, and thus $\Phi_e(t)$, can then be expressed in terms of V_d by inversion of (5), with $h(V_d)$ being obtained as the only real root of the cubic equation, giving:

$$h(V_d) = \frac{\alpha^2 - 12u}{\alpha} \tag{6}$$

where

$$\alpha := \sqrt[3]{108v + 12\sqrt{12u^3 + 81v^2}} \tag{7}$$

85 and

$$u := 3r_0^2, \quad v := \frac{6V_d}{\pi} \tag{8}$$

The above already permits calculating the droplet size (e.g., in terms of the droplet radius $r(t) = \left(r_0^2 + h(t)^2\right)/(2h))$ and the evaporative water flux $\Phi_e(t)$, both as a function of the time-dependent input water flux $\Phi_0(t)$, by numerical integration of Eq. (3).

90 Going one step further we include a second mass balance equation in the model to account for the rare isotopologues (in practice either ^{2}H^{16}O^{1}H or ^{1}H^{18}O^{1}H). We start with expressing the rare isotope fluxes (identified by $\star$) in terms of the total fluxes and the isotope ratio of the reservoir in question. For the three relevant fluxes (see Figure 1):

$$\Phi_0^\star = \Phi_0 \frac{R_0}{1 + R_0} = \Phi_0 \frac{R_{VSMOW}(1 + \delta_0)}{1 + R_{VSMOW}(1 + \delta_0)} \tag{9}$$

$$\Phi_c^\star = \Phi_c \frac{R_0}{1 + R_0} = \Phi_c \frac{R_{VSMOW}(1 + \delta_0)}{1 + R_{VSMOW}(1 + \delta_0)} \tag{10}$$

95 $$\Phi_e^\star = \Phi_e \frac{R_s \alpha_{eff}}{1 + R_s \alpha_{eff}} = \Phi_e \frac{R_{VSMOW}(1 + \delta_0)\alpha_{eff}}{1 + R_{VSMOW}(1 + \delta_0)\alpha_{eff}} \approx \Phi_e \frac{R_{VSMOW}(1 + \delta_0)\alpha_{eff}}{1 + R_{VSMOW}(1 + \delta_0)} \tag{11}$$

Here R_w is the ratio of the abundance of the rare to the most abundant water isotope in the reservoir w ($w = 0, c, s, e$ for respectively, the syringe and needle, the core of the droplet, droplet surface layer, and the evaporated water) (e.g., $^2R_s = \left(\left[^2\text{H}\right]/\left[^1\text{H}\right]\right)_s$). R_{VSMOW} is the isotope ratio of the international standard material Vienna Standard Mean Ocean Water (IAEA, 2017), and $\delta_w := (R_w - R_{VSMOW})/R_{VSMOW}$, the relative deviation of the abundance ratio in reservoir w with respect

100 to that of VSMOW. Finally, the fractionation factor between the (evaporated) vapor phase water and the liquid $\alpha_{eff} \approx 1$ ($\epsilon_{eff} \ll 1$), making the approximation made in Eq. (11) a very good one.

Similar equations as (9), (10), and (11) hold for the different water reservoir volumes, allowing us to write for the volume of the isotopically enriched evaporating surface layer:

$$V_s(t + dt)\frac{R_s(t + dt)}{1 + R_s(t + dt)} = V_s(t)\frac{R_s(t)}{1 + R_s(t)} + \left(\Phi_c(t)\frac{R_0}{1 + R_0} - \Phi_e^\star(t)\right)dt \tag{12}$$

105 Substitution of:

$$\Phi_c(t) = \Phi_0(t) - \frac{dV_c(t)}{dt} = \Phi_0(t) - \frac{dV_d(t) - dV_s(t)}{dt} \tag{13}$$

And using the definition:

$$\psi(t) := \frac{R_s(t)}{1 + R_s(t)} \tag{14}$$

then yields:

110

$$\psi(t+dt) := \frac{1}{V_s(t+dt)} \left\{ V_s(t)\psi(t) + \left(\left(V_s(t+dt) - V_s(t) \right) - \left(V_d(t+dt) - V_d(t) \right) \right) \frac{R_0}{1+R_0} + \left(\Phi_0(t)\frac{R_0}{1+R_0} - \Phi_e(t)\psi(t)\alpha_{eff} \right) dt \right\} \quad (15)$$

where we have used the approximation for $\Phi_e^\star(t)$ of Eq. (11).

We can now calculate the isotope ratio in the enriched fraction f of the droplet volume (using Eq. (1) and an appropriate

115 value of f) by integrating Eq. (15), while evaluating Eq. (1) to (4) at each time step. The isotope ratio of the evaporated water

is then obtained as:

$$\delta_e(t) = \alpha_{eff}\left(1+\delta_s(t)\right) - 1 \quad (16)$$

with:

$$\delta_s(t) = \frac{R_s(t)}{R_{VSMOW}} - 1 \quad (17)$$

120 and:

$$R_s(t) = \frac{\psi(t)}{1+\psi(t)} \quad (18)$$

3 Results

The above model has been programmed in Mathcad (PTC Mathcad, 2020) and used to simulate data that were recorded with

a home-built, low-humidity water isotope spectrometer, named HiFi, described in Landsberg (2014) and Landsberg et al.

125 (2014). Since we are specifically interested in the dynamic behavior of the water vapor source that feeds the spectrometer,

we need to take the response time of the spectrometer into account. This response is typically described by a double or even

triple exponential. At humidity levels of several thousand ppmv (parts per million by volume) the initial (fast) response time

of the bare spectrometer was determined to be in the range of 1 to 2 s for both the water concentration and the isotope

ratios, with a second, slower exponential response of the order of 15 s. However, in the configuration of this study, and

130 at the low water concentrations of a few hundred ppmv, the response time is significantly longer, especially for the δ^2H

isotope ratio. These response times were measured using as a humidity source a predecessor of the isotopic humidity generator

described in Leroy-Dos Santos et al. (2020), which was, however, equipped with two independent syringe pumps, enabling

rapid switching between two different water sources using a 2-position, 4-port valve (Valco EUDA-4UWE) just before the

spectrometer (Landsberg, 2014). The humidified air stream was sent either to the spectrometer or to a waste pump. The isotope

135 response was determined by switching between two very different water standards, assuring a high signal-to-noise-ratio of

the measurements, while keeping the concentration constant at about 600 ppmv. The standard waters used were left-over

Table 1. Parameters of the double exponential fit to the measured instrument response for δ^{18}O and δ^{2}H. The water concentration is observed to closely follow the δ^{18}O behavior and was modeled with the δ^{18}O parameters.

	τ_1 (s)	A_1	τ_2 (s)	A_2
δ^{18}O, [H$_2$O]	9.2	0.88	104	0.12
δ^{2}H	21	0.80	145	0.20

working standards of the Groningen Center for Isotope Research, known as GS-48 (δ^{18}O$= -6.3‰, \delta^{2}$H$= -43‰$) and BEW-2 (δ^{18}O$= 795‰, \delta^{2}$H$= 5983‰$).
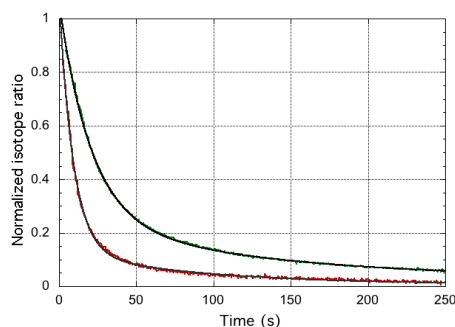
Figure 2. The normalized response curves of the spectrometer for switching between the GS-48 and BEW-2 isotope standards, both prepared as a mixture of $\sim$600 ppmv water vapor in dry air. The experimental data is fit with a double exponential yielding for the fast decay times 9.2 s and 20.7 s for δ^{18}O (red curve) and δ^{2}H (green curve), respectively.

The instrument isotope response curves are shown in Figure 2, while the double exponential fit parameters are summarized
140   in Table 1. Whereas the total water concentration and δ^{18}O show practically the same time response, δ^{2}H is about twice as slow, due to different time constants for the surface adsorption processes. Although at much higher humidity, Steen-Larsen et al. (2014) observed a qualitatively similar behavior. In the following sections, the time response of the spectrometer is taken into account by convolution of the simulated response of the humidity generator with the calculated impulse response of the spectrometer before comparison to the corresponding experimental data. For all measurements shown here, the water isotope
145   analyzer was calibrated with respect to the same water standard (GS-48) used for the measurements, resulting in relative isotope deviations (δ-values) equal to zero in steady-state conditions.

3.1 Humidity and isotope step responses

The model detailed in section 2 was first used to simulate the dynamic behavior of the combination of the LHLG and the HiFI isotope analyzer, while the LHLG was programmed to generate small humidity steps of about 200 ppmv around an absolute

150 value of roughly 400 ppmv. The simulated water concentration response was fit to the experimental data by adjusting the evaporation rate k_e, the only free parameter in this case (see the top panel of Fig. 3). We will discuss the rationale for the values of k_e determined in our study later in section 4.4. Having fixed the evaporation rate at an optimal value of $k_e = 3\ \mu\text{m/s}$, the next step is to confirm that the isotope responses are modeled correctly, taking into account that both the $\delta^2\text{H}$ and $\delta^{18}\text{O}$ simulated responses also depend on the fraction f of the droplet volume that becomes enriched, as well as the effective liquid-to-vapor

155 fractionation factor α_{eff}. Since we expect the entire droplet to become enriched in the heavy isotopologues, we start with the assumption that $f = 1$. As we will see shortly, this choice is validated by the experimental observations. It will subsequently be rationalized by theoretical considerations in section 4.1.
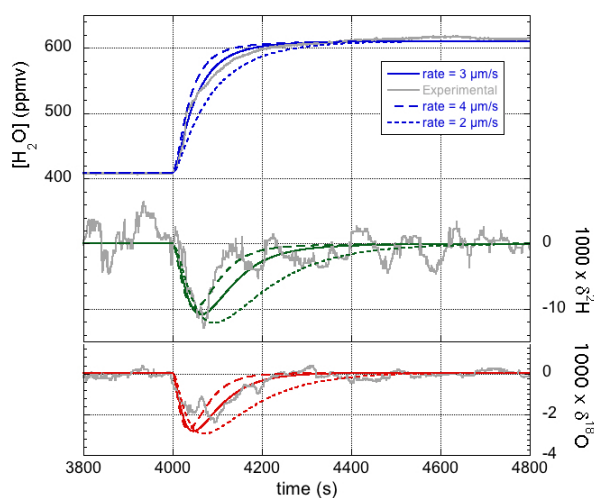
Figure 3. Experimental data (gray curves) and model simulations of the humidity (blue traces, top panel) and isotope response curves (green for $\delta^2\text{H}$ and red for $\delta^{18}\text{O}$, lower panel) for three different values of the evaporation rate k_e. The best fit is obtained for $k_e \approx 3\ \mu\text{m/s}$, whereas a higher (lower) value results in a simulated dynamic response that is too fast (slow) compared to the measured response.

As to the fractionation factors, we consider that at the very low relative humidity of our experiment ($h \approx 0.01$), the effective fractionation factors α_{eff} can be written as the product of a diffusion fractionation factor α_{diff} and an equilibrium fraction-

160 ation factor α_{eq} (Cappa et al., 2003). Moreover, the diffusion fractionation factor can be related to the ratio of the molecular

Table 2. Effective fractionation factors as a function of the flow parameter n. For $n = 0$ the fractionation factors are equal to the equilibrium values at 35 °C, such as they were determined by Horita and Wesolowski (1994).

n	0	0.43	1
	turbulent	intermediate	laminar
$^2\alpha_{eff}$	0.9370	0.9288	0.9181
$^{18}\alpha_{eff}$	0.9915	0.9800	0.9650

diffusivities (Stewart, 1975), such that we may write:

$$^x\alpha_{eff} = {}^x\alpha_{eq} \left(\frac{D(x)}{D(a)} \right)^n \tag{19}$$

Here the label x refers to the rare isotope or isotopologue (^{2}H and ^{18}O or ^{2}H^{16}O^{1}H and ^{1}H$_2^{18}$O) and a to the abundant isotope or isotopologue (^{1}H and ^{16}O or ^{1}H$_2^{16}$O). The effective fractionation factors for ^{2}H^{16}O^{1}H and ^{1}H$_2^{18}$O are thus not independent, but are determined by the single parameter n. The exponent n in (19) equals unity in the case of laminar flow, and zero in the case of fully turbulent flow. The equilibrium fractionation factors were accurately determined by Horita and Wesolowski (1994), and we take their values at 35 °C. The diffusivities were determined by Cappa et al. (2003) and more recently by Luz et al. (2009). We will use the more recent values, but the difference is minimal for our purpose (Cappa et al. (2003) predict only slightly lower values of α_{eff} in the laminar limit of $n = 1$). Table 2 gives the values of the effective liquid-to-vapor fractionation factors for three different values of the flow parameter n and Fig. 4 shows the corresponding model simulations compared to experimental data. The δ^{18}O simulation shows a relatively large effect of changing n than the δ^2H simulation. In contrast, changing the values of f has the same relative effect on both simulations (not shown in 4). With $n = 0.43$ and $f = 1$ a good fit to both isotope response curves is obtained. We thus also conclude that our data supports the theoretical finding (section 4.1) that $f = 1$.
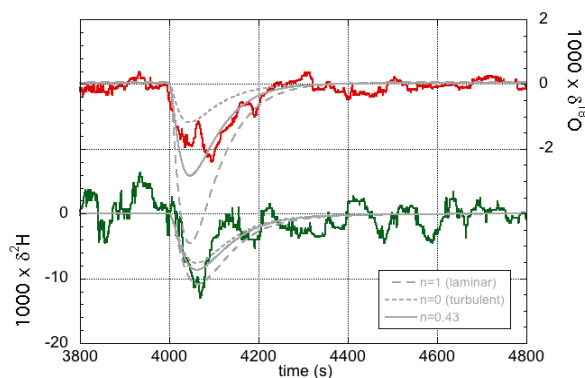
Figure 4. Experimental data and model simulations of the isotope response curves for three different values of the flow parameter n. $n = 0$ (dotted gray lines) corresponds to the turbulent flow limit, while $n = 1$ (dashed gray lines) corresponds to the limit of laminar flow. For $n = 0.43$ (solid gray lines) a good fit is obtained for both isotopes.

3.2 Dynamic response under non-ideal conditions

The LHLG was modified immediately following the experiments presented in the previous section. Notably, it was deemed that the bore of the aluminum injector chamber that accepts the syringe's needle was too narrow. With an internal diameter of only 2 mm, careful guiding of the needle, and consequently a precise positioning of the syringe, was needed to avoid occasional contact of the droplet with the chamber wall. This also limited the maximum droplet size, and therewith the volume mixing ratio (humidity level) that could be attained to roughly 1000 ppmv. The injection chamber was therefore replaced by a stainless steel sample cylinder with volume 75 mL and Sulfinert hydrophobic coating (Restek 304L-HDF4-75). Because the flow velocity is now significantly lower, the coating serves to minimize the memory effect due to surface adsorption of water molecules. In addition, a section of PTFE tubing was added between the syringe (Hamilton 84853) and the removable needle to make the alignment better manageable. This gave initially rise to unexpected results that were attributed to the appearance of small air bubbles in the water injection line. These problems were later resolved by re-engineering the LHLG as described in Leroy-Dos Santos et al. (2020). But we report on these "useless" results here because they nicely demonstrate the ability of the model to simulate the behavior of this non-ideal instrument, and thus validate the model under a different operating regime.

During similar experiments as reported in the previous section 3.1, recording the response of the LHLG following small steps in the flow of injected water, relatively large sinusoidal oscillations were observed with a period that matched the revolution speed of the lead screw of the precision pump. We submit that these oscillations become prominently visible when small imperfections of the lead screw combine with small air bubbles present in the water injection line, possibly amplified by viscous resistance of the liquid inside the water line and needle. Whatever the precise underlying mechanics, we modeled a sinusoidal variation of the water flow with a period equal to one revolution of the screw drive. The amplitude and phase of the

(possibly amplified) lead screw imperfection was chosen to yield a simulation that best matched the observed amplitude of the

195   oscillations. The only other parameter that needed adjustment was the evaporation rate. The value of $k_e = 1$ μm/s was found

to produce a simulation that best matched the water concentration response when the pump was switched between different

water flow rates, as seen in the upper panel of Fig. 5. The lower evaporation is due to the lower flow velocity of the air around

the droplet (see section 4.4).
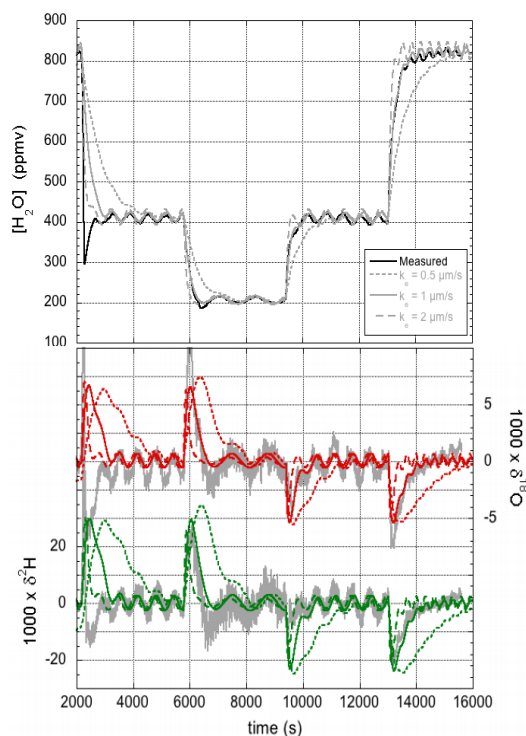
Figure 5. Humidity (upper panel) and isotope responses (lower panel) of the modified LHLG subject to stepwise changes in the water

flow rate. The best fit is obtained for an evaporation rate $k_e = 1$ μm/s. The overshoot in the first downward humidity transition and the

corresponding inverted isotope response are most likely due to an air bubble in the water line.

The corresponding response of the isotope ratios is shown in the lower panel of Fig. 5. It may be clear that the correspondence

200   between simulation and experiment is (already) satisfactory, considering that no further parameter adjustments were made. We

will further refine the simulation in the Discussion section 4.3.

4 Discussion

4.1 Droplet isotopic enrichment

Here we provide support for the observation of an enrichment in the heavy isotopologues of the entire droplet, and not just in a surface layer of limited thickness. Referring to Fig. 4 (for which $n = 0.43$, i.e., $^{18}\alpha_{eff} = 0.98$, and $f = 1$), in principle the same amplitude of the modeled response can be obtained by assuming fully laminar flow ($n = 1$), ánd assuming that a much smaller fraction of the droplet becomes enriched in the heavy isotopes. This gives, however, a less satisfactory fit to the data, as shown in Fig. 6. Notably, the response simulated with $n = 1$ (i.e., $^{18}\alpha_{eff} = 0.9650$) and $f = 0.5$, reached the same maximum amplitude, but is clearly narrower than the experimental curve. Importantly, this is also not what is predicted based on the speed of isotopic diffusion in the droplet.
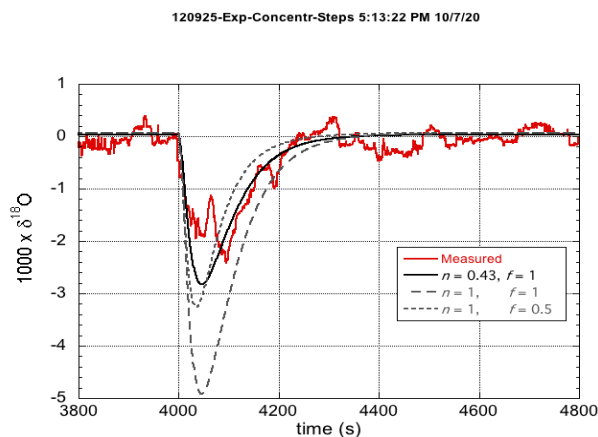
Figure 6. Experimental data and model simulations of the ^{18}O response curves for two different values of α_{eff} and two different values of f.

To see that in our experiment f should be equal to unity we consider that the enrichment occurring at the surface of the droplet will diffuse inwards, resulting in an isotope gradient inside the droplet with a characteristic diffusion length given by Bird et al. (2006):

$$L = 2\sqrt{D \cdot t} \tag{20}$$

with D the diffusion coefficient and t time. Differentiation of (20) yields the velocity of the diffusion front:

$$v_{diff} = \sqrt{\frac{D}{t}} \tag{21}$$

The diffusion coefficients of HDO and $H^{18}OH$ in water have been measured by Horita and Cole to be 2.34 10^{-9} m^2/s and 2.66 10^{-9} m^2/s, respectively (Horita and Cole (2004)). This shows that diffusion over lengths comparable to the size of a typical

droplet (0.1 mm) takes place on a time scale of the order of 1 s. It is therefore likely that the entire droplet becomes isotopically
220 enriched, rather than just a surface layer: $f = 1$.

4.2 Back Diffusion

The question arises whether the diffusion is strong enough to allow the isotopic enrichment to propagate all the way to the
syringe reservoir. To answer this question we compare the diffusion velocity of (21) to the flow velocity inside the syringe
needle:

225
$$v_{flow} = \frac{\Phi_0}{A_0} \tag{22}$$

with Φ_0 the water flux through the syringe needle and A_0 the needle's internal cross sectional area. After a characteristic
time t_e, the diffusion velocity will have become smaller than the flow velocity, at which point in time the diffusion front does
not further penetrate into the needle. This characteristic time equals:

$$t_e = D \left(\frac{A_0}{\Phi_0} \right)^2 \tag{23}$$

230 With typical values for our instrument (an inner diameter of 464 μm for the gauge 26 needle and a low water flux of about 100
nL/min), the flow velocity inside the needle is about 0.6 mm/min, such that $t_e \approx 25$ s. Eq. (20) then shows that the enrichment
propagates about 0.5 mm into the 51-mm long needle. Moreover, at the given flow rate, it takes about 600 s to arrive at the
typical droplet size of 10 μL. In this case, the isotopic diffusion into the needle thus stops already before steady-state is reached.
Even at the lowest water flow rates of about 100 pL/min, the diffusion can be stopped well within the length of the needle (if
235 necessary by reducing the needle inner diameter). We conclude that it is unlikely that the isotopic composition of the syringe
reservoir would change due to back-diffusion of heavier isotopologues. This was also confirmed experimentally by bringing
the same liquid standard material into the vapor phase with both the LHLG and a commercial humidity generator (Picarro
SDM) at time intervals of one month and not observing any difference between the measurements (within the measurement
precision of 0.2‰and 1‰for δ^{18}O and δ^2H, respectively) (Leroy-Dos Santos et al., 2020).

240 ## 4.3 Fractionation factors

The effect of the precise values of the ^{2}H^{16}O^{1}H- and H$_2^{18}$O-isotopologue effective fractionation factors on the simulations
was already discussed to some extent in section 3.1, where it was found that the best match with experiment is obtained by
assuming fractionation factors that correspond to an intermediate case between laminar and turbulent flow (characterized by
$n = 0.43$). This can be rationalized by estimating the Reynolds number for the flow around the water droplet, $R_e = \rho v L / \mu$.
245 In the previous formula $\rho \approx 1.25$ kg m^{-3} is the density of the air flowing around the needle and droplet; $v = 1.6$ m/s is the
velocity of the air around the droplet, inside the narrow-bore chamber (inner diameter 2 mm), given the air flow of 300 mL/min
(STP); $L \approx 0.5$ mm is the diameter of the droplet; and $\mu = 18.3$ μPa·s is the dynamic viscosity of air at 35 °C. We thus find
$R_e \approx 60$. This contrasts with a value of $v \approx 0.007$ m/s and $R_e \approx 0.2$ for the case of the about 30-mm internal diameter steel
cylinder used in the modified instrument. The latter case should thus be much closer to the limit of fully laminar flow. We

therefore repeat the simulations of Fig. 5, but now with the fractionation factors for $n = 1$ (see Table 2). The new simulations are shown in Fig. 7.
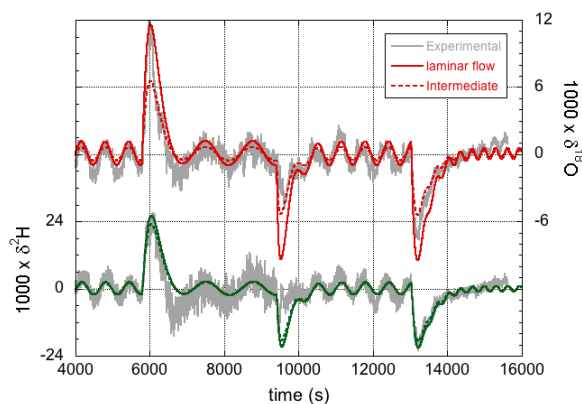
Figure 7. The isotope response of the modified LHLG subject to stepwise changes in the water flow rate. Improved simulations, compared to those of Fig. 5, are obtained with $k_e = 1$ μm/s and effective fractionation factors for the limiting case of fully laminar flow.

Whereas the differences for ^{2}H are minor, the effect of the larger ^{18}O-fractionation (i.e., smaller liquid-to-vapor fractionation factor) in the laminar flow regime is clearly visible, and arguably provides a slightly better fit to the data, primarily during the water concentration changes, as can be seen in Fig. 7. It should be noted, however, that in the regions of oscillatory behavior in between the concentration steps, the fit could also have been nudged by adjusting the amplitude of the lead screw modulation. Still, we conclude that the results of section 3.2 are just as well, and most likely better, described (than shown in Fig. 5) by assuming fully laminar flow.

4.4 Evaporation rate

The two experiments that we discussed here in sections 3.1 and 3.2 required rather different evaporation rates to simulate the data with our model, $k_e \approx 3$ μm/s and 1 μm/s, respectively. The difference is clearly related to the different Reynolds numbers or, more directly, the different dry air flow velocities of 1.6 m/s and 0.007 m/s. In fact, the values are in reasonable agreement with the results reported by Walton (2004). Although his measurements were recorded at only a small number of air temperatures and flow velocities, we can estimate values applicable to our situation by linear extrapolation of the observed rates as a function of flow velocity, and fitting a (weakly) quadratic dependence on the temperature to the data collected at a fixed flow velocity of 1 m/s. In Fig. 8 we present selected data of Walton together with the estimated values for our case. We thus predict a rate of 5.2 μm/s at a flow velocity $v = 1.6$ m/s, and of 1.3 μm/s at $v = 0$ m/s, higher than the values we found experimentally. So far we have assumed that the droplet is at the same temperature as the evaporation chamber, but it cannot be excluded that the actual droplet temperature is lower, especially in the high velocity case. However, the study by Sefiane et al.

(2009) measured an evaporation rate at 22 °C and 1 bar corresponding to ~ 4 μm/s, very close to the value we extrapolated
270   from the data of Walton (2004) at 25 °C. It should also be mentioned that it is unlikely that the difference with the observations
by Walton or Sefiane are due to an under-estimation of the spectrometer humidity response time, as it is difficult to imagine a
water concentration time response slower than that of the isotope ratios.
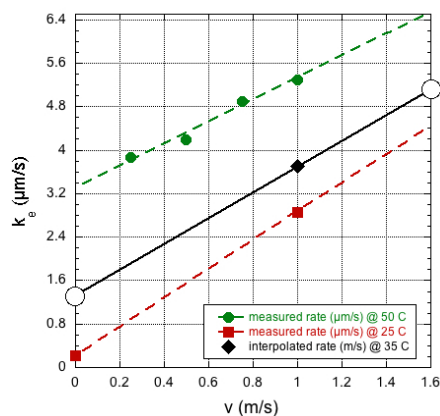
Figure 8. Evaporation rate measurements made by Walton (2004) as a function of flow velocity at 25 °C (red solid squares) and at 50 °C
(green solid circles) and one interpolated point at 35 °C (black solid diamond), leading to the extrapolated estimates for our experiment (open
circles).

5   Conclusions

We have shown that the dynamic behavior of a humidity generator based on droplet evaporation can be accurately modeled.
275   Confrontation with experimental data of the water concentration and two isotopic ratios as a function of the injected water
flow, enables the determination of physically realistic values of the droplet evaporation rate and the liquid-to-vapor isotope
fractionation factors. However, the signal-to-noise ratio of the analyzer at the very low humidity levels investigated is not
quite sufficient to make very precise determinations of the fractionation factors. But recent developments in ultra-precise and
ultra-sensitive isotope measurements (e.g., Stoltmann, 2017; Kassi et al., 2018) will enable to deliver more precise values
280   by at least an order of magnitude. What may appear as a bit of a quixotic study of evaporating water droplets, may thus in
fact permit measuring not only the evaporation rate, but also the effective fractionation factors, and therewith also isotopologue
dependent diffusivity ratios, in the evaporation of small sessile droplets. Apart from this potentially new application, it is highly
satisfactory to be able to accurately simulate the dynamic behavior of the LHLG with few free parameters, and under rather
different operating conditions.

285 *Code availability.* Please contact the author if you wish to obtain a copy of the Mathcad code.

Author contributions. EK developed the model and Mathcad code, and applied these to the data obtained in Grenoble using instrumentation built by Janek Landsberg and EK.

Competing interests. The author declares to not have any competing interests.

Acknowledgements. I am indebted to past and present colleagues and students. In particular, Janek Landsberg was instrumental in building
290 the prototype humidity generator, with valuable contributions coming from Daniele Romanini and Samir Kassi. Janek Landsberg and Marine Favier recorded some of the experimental data shown here. Amaelle Landais provided valuable feedback on the manuscript.

References

Bird, R. B., Stewart, W. E., and Lightfoot, E. N.: Transport Phenomena, John Wiley & Sons, revised 2n edn., 2006.

Bréant, C., Leroy Dos Santos, C., Agosta, C., Casado, M., Fourré, E., Goursaud, S., Masson-Delmotte, V., Favier, V., Cattani, O., Prié, F., Golly, B., Orsi, A., Martinerie, P., and Landais, A.: Coastal water vapor isotopic composition driven by katabatic wind variability in summer at Dumont d'Urville, coastal East Antarctica, Earth and Planetary Science Letters, 514, 37–47, https://doi.org/10.1016/j.epsl.2019.03.004, https://doi.org/10.1016/j.epsl.2019.03.004, 2019.

Cappa, C. D., Hendricks, M. B., DePaolo, D. J., and Cohen, R. C.: Isotopic fractionation of water during evaporation., J. Geophys. Res., 108, doi: 10.1029/2003JD003 597, 2003.

Casado, M., Landais, A., Masson-Delmotte, V., Genthon, C., Kerstel, E., Kassi, S., Arnaud, L., Picard, G., Prie, F., Cattani, O., Steen-Larsen, H.-C., Vignon, E., and Cermak, P.: Continuous measurements of isotopic composition of water vapour on the East Antarctic Plateau, Atmospheric Chemistry and Physics, 16, 8521–8538, https://doi.org/10.5194/acp-16-8521-2016, https://www.atmos-chem-phys.net/16/8521/2016/, 2016.

Gkinis, V., Popp, T. J., Johnsen, S. J., and Blunier, T.: A continuous stream flash evaporator for the calibration of an IR cavity ring-down spectrometer for the isotopic analysis of water, Isotopes in Environmental and Health Studies, 46, 463–475, http://www.informaworld.com/10.1080/10256016.2010.538052, 2010.

Horita, J. and Cole, D. R.: Stable isotope partitioning in aqueous and hydrothermal systems to elevated temperatures, in: Aqueous Systems at Elevated Temperatures and Pressures, edited by Palmer, D. A., Fernández-Prini, R., and Harvey, A. H., chap. 9, pp. 277–319, Elsevier, London, https://doi.org/10.1016/B978-012544461-3/50010-7, http://www.sciencedirect.com/science/article/pii/B9780125444613500107https://linkinghub.elsevier.com/retrieve/pii/B9780125444613500107, 2004.

Horita, J. and Wesolowski, D. J.: Liquid-vapor fractionation of oxygen and hydrogen isotopes of water from the freezing to the critical temperature., Geochimica Et Cosmochimica Acta, 58, 3425–3437 [1–2, 6–2], 1994.

IAEA: Reference Sheet for VSMOW2 and SLAP2 International Measurement Standards, Tech. rep., Department of Nuclear Sciences and Applications IAEA Environment Laboratories, Vienna, 2017.

Iannone, R. Q., Kassi, S., Jost, H.-J., Chenevier, M., Romanini, D., Meijer, H. A. J., Dhaniyala, S., Snels, M., and Kerstel, E.: Development and airborne operation of a compact water isotope ratio infrared spectrometer., Isotopes in environmental and health studies, 45, 303–320, https://doi.org/10.1080/10256010903172715, http://www.ncbi.nlm.nih.gov/pubmed/19670069, 2009a.

Iannone, R. Q., Romanini, D., Kassi, S., Meijer, H. A. J., and Kerstel, E. R. T.: A Microdrop Generator for the Calibration of a Water Vapor Isotope Ratio Spectrometer, Journal of Atmospheric and Oceanic Technology, 26, 1275–1288, https://doi.org/10.1175/2008JTECHA1218.1, http://journals.ametsoc.org/doi/abs/10.1175/2008JTECHA1218.1, 2009b.

Iannone, R. Q., Romanini, D., Cattani, O., Meijer, H. A. J., and Kerstel, E.: Water isotope ratio ($\delta 2H$ and $\delta 18O$) measurements in atmospheric moisture using an optical feedback cavity enhanced absorption laser spectrometer, Journal of Geophysical Research, 115, 1–12, https://doi.org/10.1029/2009JD012895, http://www.agu.org/pubs/crossref/2010/2009JD012895.shtml, 2010.

Kassi, S., Stoltmann, T., Casado, M., Daëron, M., and Campargue, A.: Lamb dip CRDS of highly saturated transitions of water near 1.4 μm, Journal of Chemical Physics, 148, https://doi.org/10.1063/1.5010957, http://dx.doi.org/10.1063/1.5010957, 2018.

Kerstel, E.: Isotope ratio infrared spectrometry., in: Handbook of stable isotope analytical techniques, edited by De Groot, P. A., vol. 1, chap. 34, pp. 759–787, Elsevier (Amsterdam), 2004.

Kerstel, E. and Gianfrani, L.: Advances in laser-based isotope ratio measurements: selected applications, Applied Physics B-Lasers and
    Optics, 92, 439–449, https://doi.org/10.1007/s00340-008-3128-x, 2008.

330   Landsberg, J.: Development of a water vapor isotope ratio infrared spectrometer and application to measure atmospheric water in Antarctica,
    Ph.D. thesis, Université Grenoble Alpes, 2014.

Landsberg, J., Romanini, D., and Kerstel, E.: Very high finesse optical-feedback cavity-enhanced absorption spectrometer for low concen-
    tration water vapor isotope analyses, Optics Letters, 39, 1795–1798, https://doi.org/10.1364/OL39.001795, 2014.

Leroy-Dos Santos, C., Casado, M., Prie, F., Jossoud, O., Kerstel, E., Kassi, S., Fourre, E., and Landais, A.: A dedicated robust instrument

335   for water vapor generation at low humidity for use with a laser water isotope analyzer in cold and dry polar regions., Atmos. Meas. Tech.
    Discuss., in review, https://doi.org/10.5194/amt-2020-345, 2020.

Luz, B., Barkan, E., Yam, R., and Shemesh, A.: Fractionation of oxygen and hydrogen isotopes in evaporating water, Geochim-
    ica et Cosmochimica Acta, 73, 6697–6703, https://doi.org/10.1016/j.gca.2009.08.008, http://linkinghub.elsevier.com/retrieve/pii/
    S0016703709005110, 2009.

340   Moyer, E. J., Sarkozy, L., Lamb, K., Clouser, Stutz, E., Kühnreich, B., Landsberg, F., Habig, J. C., Hiranuma, N., Wagner, S., Ebert, V., Kers-
    tel, E., Möhler, O., and Saathoff, H.: Applications of Absorption Spectroscopy for Water Isotopic Measurements in Cold Clouds, in: Min-
    eralogical Magazine, vol. 77, pp. 1661–1817, http://openurl.ingenta.com/content/xref?genre=article{&}issn=0026-461X{&}volume=
    77{&}issue=5{&}spage=1661, 2013.

PTC Mathcad: MathCAD: Math software for engineering calculations, https://www.mathcad.com/en, accessed: 2020-09-30, 2020.

345   Ritter, F., Steen-Larsen, H. C., Werner, M., Masson-Delmotte, V., Orsi, A., Behrens, M., Birnbaum, G., Freitag, J., Risi, C., and Kipfstuhl, S.:
    Isotopic exchange on the diurnal scale between near-surface snow and lower atmospheric water vapor at Kohnen station, East Antarctica,
    The Cryosphere Discussions, pp. 1–35, https://doi.org/10.5194/tc-2016-4, 2016.

Sefiane, K., Wilson, S. K., David, S., Dunn, G. J., and Duffy, B. R.: On the effect of the atmosphere on the evaporation of sessile droplets of
    water, Physics of Fluids, 21, 1–31, https://doi.org/10.1063/1.3131062, 2009.

350   Steen-Larsen, H. C., Masson-Delmotte, V., Hirabayashi, M., Winkler, R., Satow, K., Prié, F., Bayou, N., Brun, E., Cuffey, K. M., Dahl-
    Jensen, D., Dumont, M., Guillevic, M., Kipfstuhl, J., Landais, A., Popp, T., Risi, C., Steffen, K., Stenni, B., and Sveinbjörnsdottír, A.: What
    controls the isotopic composition of Greenland surface snow?, Climate of the Past Discussions, 9, 6035–6076, https://doi.org/10.5194/cpd-
    9-6035-2013, http://www.clim-past-discuss.net/9/6035/2013/, 2013.

Steen-Larsen, H. C., Sveinbjörnsdottir, A. E., Peters, A. J., Masson-Delmotte, V., Guishard, M. P., Hsiao, G., Jouzel, J., Noone, D., Warren,

355   J. K., and White, J. W.: Climatic controls on water vapor deuterium excess in the marine boundary layer of the North Atlantic based on
    500 days of in situ, continuous measurements, Atmospheric Chemistry and Physics, 14, 7741–7756, https://doi.org/10.5194/acp-14-7741-
    2014, 2014.

Stewart, M. K.: Stable isotope fractionation due to evaporation and isotopic exchange of falling waterdrops: Applications to atmospheric
    processes and evaporation of lakes, Journal of Geophysical Research, 80, 1133–1146, https://doi.org/10.1029/JC080i009p01133, http:

360   //doi.wiley.com/10.1029/JC080i009p01133, 1975.

Stoltmann, T.: Development and applications of a laser spectrometer dedicated to the measurement of isotopic anomalies in carbon dioxide,
    Ph.D. thesis, Universite Grenoble Alpes, 2017.

Sturm, P. and Knohl, A.: Water vapor 2H and 18O measurements using off-axis integrated cavity output spectroscopy, Atmospheric Mea-
    surement Techniques, 3, 67–77, https://doi.org/www.atmos-meas-tech.net/3/67/2010/, 2010.

365   Tremoy, G., Vimeux, F., Cattani, O., Mayaki, S., Souley, I., and Favreau, G.: Measurements of water vapor isotope ratios with wavelength-scanned cavity ring-down spectroscopy technology: new insights and important caveats for deuterium excess measurements in tropical areas in comparison with isotope-ratio mass spectrometry., Rapid Comm. Mass Spectrom., 25, 3469–3480, 2011.

Walton, D. E.: The Evaporation of Water Droplets. A Single Droplet Drying Experiment, Drying Technology, 22, 431–456, https://doi.org/10.1081/DRT-120029992, http://www.tandfonline.com/doi/abs/10.1081/DRT-120029992, 2004.